

THE GLOBULAR CLUSTER SYSTEMS AROUND NGC 3311 AND NGC 3309

ELIZABETH M. H. WEHNER

Department of Physics & Astronomy, McMaster University, Hamilton L8S 4M1, Canada

WILLIAM E. HARRIS

Department of Physics & Astronomy, McMaster University, Hamilton L8S 4M1, Canada

BRADLEY C. WHITMORE

Space Telescope Science Institute, 3700 San Martin Drive, Baltimore MD 21218

BARRY ROTHBERG

Space Telescope Science Institute, 3700 San Martin Drive, Baltimore MD 21218

KRISTIN A. WOODLEY

Department of Physics & Astronomy, McMaster University, Hamilton L8S 4M1, Canada

Draft version May 26, 2018

ABSTRACT

We present extensive new photometry in (g', i') of the large globular cluster (GC) system around NGC 3311, the central cD galaxy in the Hydra cluster. Our GMOS data cover a $5\frac{1}{5}$ field of view and reach a limiting magnitude $i' \simeq 26.0$, about 0.5 magnitude fainter than the turnover point of the GC luminosity function. We find that NGC 3311 has a huge population of $\simeq 16,000$ GCs, closely similar to the prototypical “high specific frequency” Virgo giant M87. The color-magnitude distribution shows that the metal-poor “blue” GC sequence and the metal-richer “red” sequence are both present, with nearly equal numbers of clusters. Bimodal fits to the color distributions confirm that the blue sequence shows the same trend of progressively increasing metallicity with GC mass that has previously been found in many other large galaxies; the correlation we find corresponds to a scaling of GC metallicity with mass of $Z \sim M^{0.6}$. By contrast, the red sequence shows no change of mean metallicity with mass, but it shows an upward extension to much higher than normal luminosity into the UCD-like range, strengthening the potential connections between massive GCs and UCDs. The GC luminosity function, which we measure down to the turnover point at $M_I \simeq -8.4$, also has a normal form like those in other giant ellipticals. Within the Hydra field, another giant elliptical NGC 3309 is sitting just $100''$ from the cD NGC 3311. We use our data to solve simultaneously for the spatial structure and total GC populations of both galaxies at once. Their specific frequencies are $S_N(N3311) = 12.5 \pm 1.5$ and $S_N(N3309) = 0.6 \pm 0.4$. NGC 3311 is completely dominant and entirely comparable with other cD-type systems such as M87 in Virgo.

Subject headings: galaxies: elliptical—galaxies: individual (NGC 3311)—galaxies: individual (NGC 3309)

1. INTRODUCTION

One of the most distinctive features of the supergiant cD-type galaxies found at the centers of rich environments is the very obvious presence of huge populations of old-halo globular clusters (GCs), often numbering above 10,000 GCs in a single system and spanning radii upwards of 100 kpc (e.g. Harris 2001). These “high specific frequency” (“high- S_N ”) globular cluster systems (GCSs) provide a platform for statistical studies of halo cluster properties that cannot be carried out in any other environment. Despite their rarity, they are therefore prime targets for both observations and interpretive modelling

on the formation and evolution of GCs and their host galaxies.

The GCSs in cD galaxies (most of which are also “Brightest Cluster Galaxies” or BCGs) have been used to identify a new correlation between GC luminosity (or mass) and color (or metallicity). While the cluster metallicity distribution function (MDF) usually has a bimodal shape (e.g. Zepf & Ashman 1993; Larsen et al. 2001; Mieske et al. 2006, among many others), recent photometric work suggests that the more metal-poor GCs (those in the “blue sequence”) have higher heavy-element abundance at progressively higher luminosity. This *mass-metallicity relation* (MMR) was first discovered in eight giant BCGs by Harris et al. (2006, hereafter H06) and in the Virgo giants M87 and NGC 4649 (Strader et al. 2006). The same trend can be seen for the GCS around the giant Sa galaxy NGC 4594 (Spitler et al.

Electronic address: wehnere@physics.mcmaster.ca
Electronic address: harris@physics.mcmaster.ca
Electronic address: whitmore@stsci.edu
Electronic address: rothberg@stsci.edu
Electronic address: woodleka@mcmaster.ca

2006), and Mieske et al. (2006) find evidence for a similar MMR in their extensive sample of Virgo Cluster Survey galaxies by combining their GC data into groups by host galaxy luminosity. As H06 discuss, a clear trace of this trend had already been found for the Fornax cD NGC 1399 by Ostrov et al. (1998) and Dirsch et al. (2003), who noted that the bright end of the GC population appeared broadly unimodal rather than bimodal. As we now realize, this effect comes about essentially because the blue and red sequences merge at the top end.

Intriguingly, the more metal-rich “red” sequence is not seen to exhibit a MMR of its own in any galaxy so far. That is, for the more metal-rich GCs, metallicity is independent of mass. The basic interpretation proposed by H06 is that the blue-sequence clusters formed primarily in dwarf-sized pregalactic clouds while the first stage of hierarchical merging was beginning. In these sites, more self-enrichment could occur within the more massive dwarfs where more of the enriched gas from supernova ejecta could be held back. These same higher-mass dwarfs would also, on average, produce the most massive GCs (Harris & Pudritz 1994). By contrast, the more metal-rich GCs on the red sequence formed later, perhaps in major mergers, and at a stage when all the material could be held in the much deeper potential well of the final big galaxy. In that stage, enrichment would have been more independent of GC mass. Mieske et al. (2006) discuss a similar view. Rothberg et al. (2007) use semi-analytic galaxy formation models to test a different approach, namely the contribution of stripped dwarf nuclei to the MMR. They find that a MMR along the blue sequence appears naturally with a standard model prescription for star formation and enrichment rates in semi-analytic models. An integral part of their interpretation is that many of the massive blue GCs are actually the dense nuclei of stripped dwarfs (dE,N or UCD objects).

Still more intriguingly, at least one clear anomaly is already known to exist: although the MMR along the blue sequence has now been found unequivocally in many galaxies, it does not seem to occur in the well studied Virgo giant NGC 4472, where both the red and blue GC sequences run vertically. This result has been confirmed in several studies and in a variety of photometric bandpasses (Geisler et al. 1996; Lee et al. 1998; Puzia et al. 1999; Rhode & Zepf 2001; Strader et al. 2006; Mieske et al. 2006). (Rothberg et al. 2007) find that increasing the efficiency of supernova feedback for heating in dwarfs can produce this effect, leaving the blue GC sequence without a MMR. But it is not yet clear what underlying physical or environmental conditions would cause this to occur. In short, the existence of the MMR is beginning to provide rich new insights into the early formation era of large galaxies.

NGC 3311, the central cD galaxy in the Hydra cluster A1060, has long been an attractive target for GCS studies because it is relatively nearby ($d = 53$ Mpc for a Hydra redshift $cz \simeq 3900$ km s⁻¹ and $H_0 = 70$ km s⁻¹ Mpc⁻¹) and has an enormously populous GCS comparable with the largest known, such as M87 in Virgo or NGC 4874 in Coma. Its ranking among the high- S_N systems was established with the early photometric survey by Harris et al. (1983). Further ground-based

imaging in the Washington system (Secker et al. 1995; McLaughlin et al. 1995) indicated that its GCS was moderately metal-rich with a hint of bimodality, and that its spatial distribution was similar to the shape of the cD envelope light. Hubble Space Telescope imaging with the WFPC2 camera (Brodie et al. 2000) in the frequently used ($V - I$) color index was employed to argue that the MDF for its clusters was more like the “standard” pattern in giant ellipticals – that is, a probable bimodal structure with metal-poor and metal-rich sequences at their usual mean metallicities. The most recently published study (Hempel et al. 2005) combined the WFPC2 (V, I) data with NICMOS imaging in F160W (approximately the H -band) to gain a first rough estimate of the metallicity and age distributions through models in the ($V - I, V - H$) two-color diagram.

None of these earlier studies have given a satisfactory picture of the system. The HST-based studies (Brodie et al. 2000; Hempel et al. 2005) are hampered by the small fields of view of WFPC2 and NICMOS, yielding very incomplete spatial coverage of this big cD galaxy, and thus relatively small GC samples to work with. By contrast, the initial study of Harris et al. (1983) in the pre-CCD photographic era covered a wide field but penetrated to only quite shallow photometric limits by today’s standards. Relatively shallow limits and photometric calibration problems also affected the first CCD-based imaging (Secker et al. 1995). To study this unusually attractive GCS further, we need to draw from a new photometric study that combines depth with wide field.

2. OBSERVATIONS AND DATA REDUCTION

As part of a new program (Gemini GS-2006A-Q-24) intended to obtain deep multicolor imaging of globular cluster systems around cD galaxies, we obtained (g', i') images of NGC 3311 and the central Hydra cluster field using the GMOS imager on Gemini South, which has a $5.5' \times 5.5'$ field of view (FOV) and a scale of $0.146''/pix$ after 2×2 binning. The raw observations were taken on the nights of 2006 February 8 and March 23, under dark skies and photometric conditions, with an average seeing of $0.5''$. In each waveband, 13 individual exposures were taken, which we then reregistered and median-combined to create the final, deep images in (g', i'). The total integration time in each filter was 3900s.

The preprocessing of the raw exposures was completed with the GEMINI package in IRAF¹. In the i' frames, a small amount of night-sky fringing was present, which we successfully removed with a calibration fringe frame from the Gemini archives. After subtracting the fringe frame and then median combining all 13 i' -band frames, the resulting fringe signal contributes only 0.3 percent to the background fluctuations.

For the photometric calibration, we used exposures of Landolt standard stars (Landolt 1992) taken adjacent to our program-field images during photometric conditions. We transformed the Landolt standard-star indices in $UBVRI$ to (g', i') using the conversion equations of

¹ IRAF is distributed by the National Optical Astronomy Observatories, which are operated by the Association of Universities for Research in Astronomy, Inc., under cooperative agreement with the National Science Foundation.

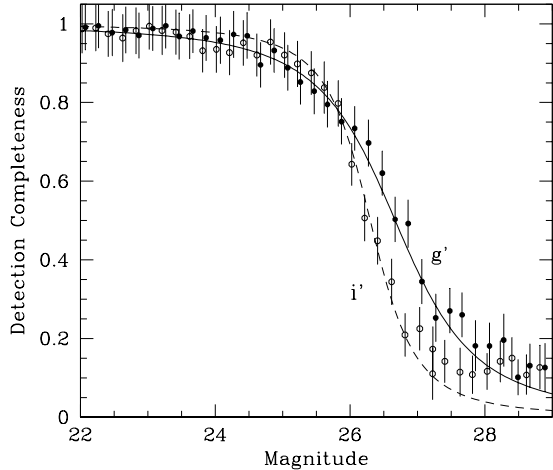


FIG. 1.— Photometric completeness of detection in g' and i' . Here the completeness fraction f , as determined from the artificial-star tests described in the text, is plotted as a function of magnitude, where $f(g')$ is plotted in the solid dots as a function of g' , and $f(i')$ is plotted in the open symbols as a function of i' . The interpolation curves drawn through each set of measurements are the two-parameter functions listed in the text.

TABLE 1
BASIC PARAMETERS FOR
NGC 3311

Parameter	Value
<i>Type</i>	E2/cD
α (J2000)	$10^{\text{h}}36^{\text{m}}42^{\text{s}}.8$
δ (J2000)	$-27^{\circ}31'42''$
v_r (helio)	3593 km s^{-1}
A_V	0.26
$(m - M)_0$	33.62
$E(g' - i')$	0.158
V_V^0	11.04
M_V^T	-22.8

Fukugita et al. (1996)². Since our standard star exposures covered only a small range in airmass, we used the NGC 3311 images taken within just the same airmass range, and taken during the same night within one hour of the standard-star exposures. This calibration was suitable only for establishing a mean zero-point value for our NGC 3311 frames, and not for a more complete evaluation of the coefficients in airmass or color. We therefore regard the calibration as only a preliminary one, to be refined when a larger network of standards can be obtained.

The final measurement of our combined, deep (g' , i') images was carried out with the latest implementation of the standalone *daophot* code, *daophot4* (Harris et al. 2007). We used an extensive series of artificial-star tests with the *addstar* component of *daophot* to evaluate the internal photometric detection completeness as a function of magnitude: stars were added to each the g' and i' images in groups of 500 over a wide range of magni-

tudes, the images were then remeasured in the same way as the original frames, and the fraction f of stars recovered in each magnitude bin was then determined. The results are shown in Figure 1. The limits of our data, defined as the magnitudes at which f drops to 0.5, are $g'(lim) = 26.67$ and $i'(lim) = 26.30$. The trend of f with magnitude is well matched by a Pritchett interpolation function (Fleming et al. 1995),

$$f = \frac{1}{2} \left[1 - \frac{\alpha(m - m_{lim})}{\sqrt{1 + \alpha^2(m - m_{lim})^2}} \right]. \quad (1)$$

which has two free parameters: the limiting magnitude m_{lim} , and a parameter α giving the steepness of the dropoff. For these images we find $\alpha_{g'} = 0.8$ and $\alpha_{i'} = 1.4$. As will be seen below, the limiting magnitudes $g'(lim) = 26.7$ and $i'(lim) = 26.3$ are deep enough to be comparable with the GC luminosity function turnover point of NGC 3311. Within the bright bulge of NGC 3311, the photometry depth diminishes due to the increased local sky noise at small radii. However, for radii larger than 0.6 from NGC 3311, which include the vast majority of our data, we find no change in the completeness limits $g', i'(lim)$.

The random uncertainties of the photometry, as determined from *daophot/allstar* and from the same artificial-star tests, are well approximated by the interpolation curves

$$\sigma(g') = 0.01 + 0.050 \exp(g' - 26.0), \quad (2)$$

$$\sigma(i') = 0.01 + 0.050 \exp(i' - 25.0). \quad (3)$$

They show little variation from place to place within the GMOS field, indicating that crowding is unimportant, and that background light from NGC 3311 and NGC 3309 has little influence except near their very centers. On the basis of these error curves, we would expect the GC sequences to start being noticeably ‘broadened’ in color, purely because of random uncertainties in the photometry, for levels $i' \gtrsim 24$. Lastly, the artificial-star tests show that any *systematic* error (net bias) in the photometry is less than 0.02 mag in each filter for $i' < 25, g' < 26$.

Throughout the following discussion we adopt a distance modulus $(m - M)_0 = 33.62$ for NGC 3311 and foreground reddening $E(g' - i') = 0.158$, as we did in Wehner & Harris (2007).

3. THE COLOR-MAGNITUDE DISTRIBUTION

After carrying out the photometry in g' and i' with *daophot* we used the additional code SExtractor (Bertin & Arnouts 1999) to help reject obvious nonstellar objects from the detection lists (at $0.5''$ seeing and at the distance of the Hydra cluster, globular clusters appear indistinguishable from the starlike PSF. Under HST-type resolution of $0.1''$, the profiles of the very biggest GCs can, however, be resolved; see Wehner & Harris 2007). Detections from the two wavebands were then correlated, and only those objects found in both were kept for the final analysis.

The final color-magnitude measurements for 8108 starlike objects across the entire GMOS field are shown in Figure 2. The globular cluster population is readily visible as the dominant concentration of points in the color range $0.6 \lesssim (g' - i') \lesssim 1.4$. Fainter than $i' \sim 25$

² A complete set of the Landolt (1992) standard stars transformed from the Johnson-Cousins system into the Sloan filter set has been compiled by the authors and is available online at <http://www.elizabethwehner.com/astro/sloan.html>

the field contamination and photometric scatter increase markedly, but brighter than this, the GC population is well defined. Evidence of the standard “blue” and “red” sequences can already be seen and will be discussed more quantitatively below through objective bimodal fits. On the red-sequence side (approximately in the range $1.0 < (g' - i') < 1.3$) a distinctive bright extension to high luminosity can be seen that, intriguingly, does not exist for the blue GC sequence. This bright-end feature extends up into the GC mass range $M \gtrsim 10^7 M_\odot$ that overlaps with the regime of the “Ultra-Compact Dwarfs” (UCDs). We have discussed these objects in our previous paper (Wehner & Harris 2007).

To date, not much other photometry of globular cluster systems in the (g', i') indices has been published that we can make comparisons with. Forbes et al. (2004) present $(g' - i')$ data taken with the GMOS camera on Gemini North for the Virgo giant NGC 4649. The bimodal fit they obtain to its GC color distribution has mean values $(g' - i')_0$ for the blue and red sequences which are ~ 0.1 mag redder than our calibrated and dereddened colors for NGC 3311. We would expect *a priori*, however, that the colors of the two sequences would be quite similar from one galaxy to the next (e.g. Harris et al. 2006; Strader et al. 2004) with only a modest trend due to the parent galaxy luminosity. For the present, we do not regard this difference as significant, because (as emphasized above) we regard our zeropoint calibration as a preliminary one, which still needs a separate series of observations especially to establish the photometric color terms. Notably, Forbes et al. also regard their own zeropoint calibration as preliminary. What is perhaps more important at this stage, and equally worth noting, is that the mean color difference $\Delta(g' - i') \simeq 0.30 \pm 0.08$ between the red and blue sequences that we find for NGC 3311 (see the discussion below) is identical with the separation between those two sequences measured for NGC 4649 by Forbes et al. (2004).

4. THE GLOBAL FEATURES OF THE GLOBULAR CLUSTER SYSTEM

In sections 4.1 – 4.2 we use our GMOS data to discuss the spatial distribution of the GCs around both NGC 3311 and 3309, including the radial and azimuthal components. A continuing theme in this analysis is the relative contribution of the two galaxies to the GC population we see on our images. In section 4.3, we discuss the color (metallicity) distribution of the GCs by radius around NGC 3311, and in sections 4.4 – 4.5 we discuss the GC luminosity function and specific frequencies.

4.1. Measuring the Radial Profiles: The NGC 3309 Problem

The core of the Hydra cluster contains several other large galaxies in addition to the central supergiant that was our primary target. Of these others, the closest in projection and by far the most luminous is the giant elliptical NGC 3309, just $100''$ away from the center of NGC 3311. Its integrated magnitude ($V_T = 11.94$; see below) places it 0.9 magnitude fainter than NGC 3311 ($V_T = 11.04$), though the true total luminosity of NGC 3311 is estimated to be about 1.3 mag brighter than that of NGC 3309 because of its extended cD envelope. Nevertheless, we might expect that NGC 3309 would con-

tribute significant numbers of GCs of its own to the population of objects in the field. By using starcounts around each of the two galaxies on the sides opposite to the other galaxy, Harris et al. (1983) and McLaughlin et al. (1995) both argued that NGC 3309 was likely to be contributing no more than a few percent of the GCs in the Hydra core field, with NGC 3311 acting as the dominant contributor. Even though NGC 3311 is clearly a high- S_N elliptical like many cDs, such claims might mean that NGC 3309 would have unusually low S_N for a giant elliptical in a rich cluster. A better and more quantitative estimate of the relative populations, as well as the spatial structures of the two GCSs, is possible from our deeper data.

To quantify our analysis, let us assume that the projected number density of GCs on the sky from each of the two galaxies can be modelled by a circularly symmetric function $\sigma(r)$ giving the number of GCs per unit projected area (we justify the assumption of symmetry below). Then, the total number density of counted objects at a point (x, y) anywhere in the field is given by

$$\sigma(x, y) = \sigma_b + \sigma_1(r_1) + \sigma_2(r_2) \quad (4)$$

where r_1 is the distance of the given point (x, y) from the center of NGC 3311, r_2 is its distance from the center of NGC 3309, and σ_1, σ_2 are the two radial functions specifying the GCS around each galaxy. Finally, σ_b is the uniform background density of whatever contaminating objects fall within our selected sample. Our goal is to deduce, from a fit to the observed GC distribution in the field, the best-estimate parameters for σ_1 and σ_2 *simultaneously*.

To perform the fit, we adopt two possible models for the distribution:

(a) A standard Hubble profile,

$$\sigma(r) = b \left(1 + \frac{r}{c}\right)^{-a} \quad (5)$$

which is a power law with an added core profile of core radius c .

(b) A generalized Sersic profile,

$$\sigma(r) = \sigma_e \exp \left[-b_n \left(\left(\frac{r}{r_e} \right)^{1/n} - 1 \right) \right] \quad (6)$$

where $b_n \simeq 1.99n - 0.3271$ (Ferrarese et al. 2006) to guarantee that r_e will be the half-light radius, and for typical E galaxies, the exponent n is found observationally to fall in the range $\simeq 1 - 4$. The case $n = 4$ recovers the standard de Vaucouleurs law.

To carry out the actual numerical fit, we divide up the observed area into $k \times k$ boxes, each of area A ; we use the model parameters to predict how many objects $N_{ij} = A \cdot \sigma(x_i, y_i)$ should be found in each box at position (x_i, y_j) , $i, j = 1, \dots, k$; and then calculate the residuals (observed – predicted) in each box. A standard goodness of fit based on Poisson statistics can then be formed,

$$\chi^2 = \sum \frac{(N_{ij}(obs) - N_{ij}(pred))^2}{N_{ij}(pred)} \quad (7)$$

The outline of the model is shown in Figure 3 for the 14×14 grid that we used for the final reductions. An advantage of this procedure is that it uses the information everywhere in the frame, not just the counts within some

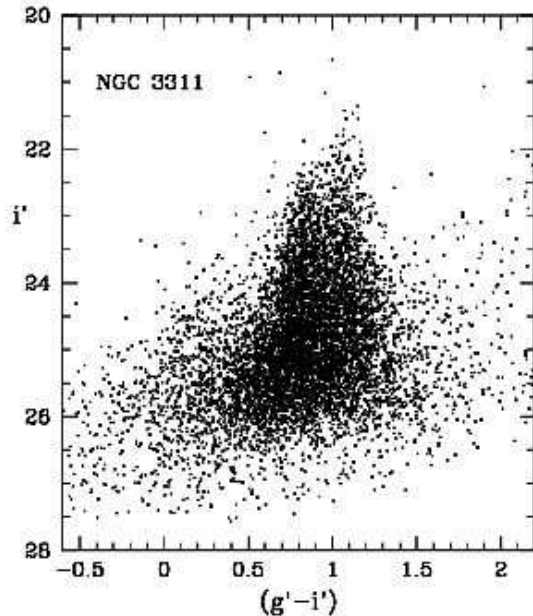


FIG. 2.— The color-magnitude diagram for all measured objects in the GMOS field centered on NGC 3311.

arbitrary radius centered on NGC 3311. In practice, we ignored any boxes located at the centers of the two galaxies and at one very bright foreground star, as well as the boxes under the shadow of the camera guide probe (lower right part of Fig. 3) and at the vignetted corners of the field. To reduce field contamination from the outset (see Fig. 2), we used the sample of 4393 objects within the restricted range $i' < 25.4$, $0.6 < (g' - i') < 1.4$, expecting that this sample would be dominated by GCs.

When we fit Eq. 4 to the data, in principle we have a total of six free parameters. For the Hubble profile model, these six are σ_b , a_1 , c_1 , a_2 , c_2 , and the relative amplitude b_1/b_2 . For the Sersic model, they are σ_b , r_{e1} , r_{e2} , n_1 , n_2 and σ_{e1}/σ_{e2} . Once a particular ratio b_1/b_2 is chosen, the actual values of both b_1 and b_2 individually are automatically set by the condition that the *total* predicted population of objects in the field must precisely equal the observed total. The same applies to σ_{e1} and σ_{e2} for the Sersic model.

In practice, the background density σ_b is extremely hard to determine by the fitting procedure alone, because the NGC 3311 GCS is so extensive that it dominates the starcounts even near the edges of our GMOS field. An external constraint on σ_b is therefore desirable. Lacking any remote “control field” to rely on, we use the distribution of stars in the CMD itself (Fig. 2) to estimate the background. The background contamination will be due to a combination of foreground Milky Way stars and faint, small remote galaxies. We can estimate the number and color distribution of possible field stars using the galactic stellar population synthesis models³ of Robin et al. (2003). Using a $5.5' \times 5.5'$ field centered on NGC 3311, the models find only 13 stars, suggesting contamination from galactic foreground stars is small at these latitudes. Using a larger field of view, such as a square degree, results in over 2 thousand stars with a color distribution leaning blueward of the blue peak

³ <http://bison.obs-besancon.fr/modele/>

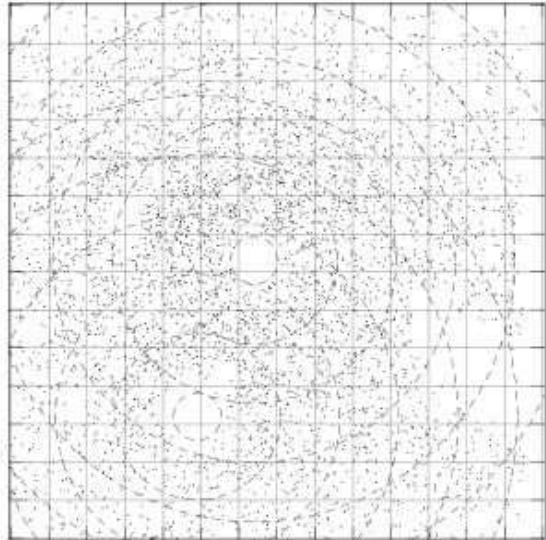


FIG. 3.— Grid layout showing the determination of the spatial structure of the GCS. Here North is at left and East at top, following the instrumental orientation of the GMOS camera during the observations. The center of NGC 3311 is near the center of the field, while the center of NGC 3309 is at lower left; the guide probe shadow is at lower right. The dots are the measured objects in the restricted range ($i' < 25.0$, $0.6 < (g' - i') < 1.4$) as described in the text. Concentric circles are drawn around each of the two major galaxies, while the grid lines show the 14×14 matrix of boxes used to solve simultaneously for the radial distributions of the GCSs around both galaxies.

of the GCS distribution. Our main source of contamination, as indicated by the initial FOV search, is most likely distant background galaxies. Without a control field, we cannot specifically quantify these background galaxies. If we assume that their distribution of colors is roughly uniform over the interval $0.0 \lesssim (g' - i') \lesssim 2.0$, we can use the numbers of objects with colors in the ranges $0.0 < (g' - i') < 0.6$ and $1.4 < (g' - i') < 2.0$ to predict how many background objects are in our selected midrange of $0.6 < (g' - i') < 1.4$. For $i' < 25.4$ we count 860 objects total that are bluer or redder than the GC color range. Normalizing to the same color interval, we then estimate that 570 of the 4393 objects within $0.6 < (g' - i') < 1.4$ (or about 13%) are background contamination, equivalent to $\sigma_b = 18 \text{ arcmin}^{-2}$. In the numerical fitting procedure we adopted this background throughout and treated only the 5 remaining parameters in each model as free.

For the Hubble profile model, we obtain a best-fit set of parameters $a_1 = -2.04 \pm 0.07$ and $c_1 = 94'' \pm 8''$ for NGC 3311; and $a_2 = -2.8(+0.7, -1.3)$ and $c_2 = 55''(+30'', -24'')$ for NGC 3309. The ratio (b_2/b_1) is 0.093 ± 0.057 . For this set of parameters the minimum reduced χ_ν value was 1.44. We experimented with different grid sizes and found that the results were not sensitive within broad limits to the fineness k^2 of the chosen grid. Given the simple nature of the model, and other factors not accounted for such as the necessarily patchy sampling across the grid, the internally uncertain adopted level of the background, and possible clumpiness (clustering) in the background population, the fit is successful at accomplishing our main goal to evaluate the relative contributions of the two giant galaxies.

A very slightly better overall fit (minimum $\chi_\nu = 1.41$)

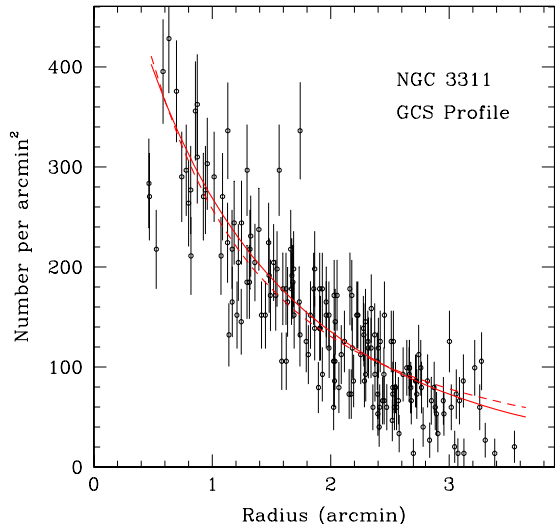


FIG. 4.— Radial distribution of the GCs in the field relative to the center of NGC 3311. The number of objects within each of the grid boxes shown in the previous figure is plotted against the radial distance of the box center from NGC 3311. The best-fitting Hubble profile (see text) is shown as the dashed line, while the best-fitting generalized Sersic model is the solid line.

is obtained with the generalized Sersic model. For the NGC 3311 GCS, we find $n_1 = 1.24 \pm 0.06$ and $r_{e1} = 177'' \pm 9''$, while for NGC 3309 $n_2 = 1.1(+1.2, -1)$ and $r_{e2} = 93''(+78'', -45'')$. The ratio of the two amplitudes is $(\sigma_{e2}/\sigma_{e1}) = 0.080 \pm 0.046$.

For comparison, the scale sizes of the underlying halo light of each galaxy are significantly smaller: Vasterberg et al. (1991) find $r_e \simeq 21''.5 \simeq 5.6$ kpc for NGC 3309 and $94''.2 \simeq 25$ kpc for NGC 3311 from an integrated-light study in the Gunn r filter. These effective radii are not strictly comparable to our solutions for the GCSs, because they assume a classic de Vaucouleurs profile ($n = 4$ in the Sersic model); but they confirm that the GCS is spatially more extended, as has usually been found for giant galaxies (McLaughlin 1999; Harris 2001).

One very evident result of this numerical exercise is that NGC 3309 contributes only a minor part of the GC population in our field (2 to 3 percent; see section 4.5 below). As a consequence, its GCS shape parameters are quite weakly constrained. Assuming that the detected objects in the field belong *entirely* to NGC 3311 and ignoring NGC 3309 completely (that is, setting $\sigma_2 \equiv 0$ in the numerical fitting) yields a minimum χ^2 negligibly worse than the two-galaxy fit. We quantify the relative importance of the two galaxies a bit further below.

A rough comparison of the two model fits is shown in Figure 4, where we simply plot the number density of objects in each grid box as a function of distance from the center of NGC 3311. The best-fit Hubble and Sersic models for NGC 3311 alone are shown overplotted, verifying the first-order description of the entire population in the field as belonging to the central cD. The same grid plot, but this time centered on NGC 3309, gives a radically different impression, similar to picking just a random point somewhere away from NGC 3311. That is, no significant concentration towards NGC 3309 is evident.

A significant improvement in this estimate of the two GCS spatial structures will be possible if a better ex-

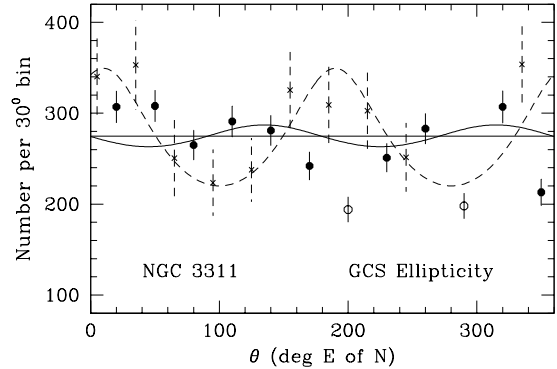


FIG. 5.— Azimuthal distribution of the GCS around NGC 3311. The numbers of objects within 30-degree sectors, and within radii $0'.26 < r < 2'.50$ of NGC 3311, are shown as the data points with error bars. The total sample includes 3544 objects divided into 30-degree sectors; the two open circles denote the sectors containing the center of NGC 3309 and the shadow of the GMOS guide probe. These are not used in the numerical fit. The sinusoid-like solid curve (see the text for the actual model curve) is the best-fitting elliptoidal model, with $\epsilon = 0.07$ and major axis $\theta_p = 90^\circ$. For comparison, the solution obtained by McLaughlin et al. (1995) from a smaller photometric sample and a brighter limit is shown by the crosses with error bars and the dashed curve.

ternal measurement of the background can be obtained. The NGC 3311 system is so extensive, however, that photometry at projected radii $r \gtrsim 10'$ (150 kpc) will be necessary for a control-field location.

4.2. Azimuthal Distributions

McLaughlin et al. (1995) also attempted to measure the ellipticity of the NGC 3311 GCS and to compare it with the shape of its cD envelope. We can, in principle, make a better test with our much larger measured population. In this case, for our test sample we take all 3544 measured objects within radii $0'.26 < r < 2'.50$ of NGC 3311 (the outer circle is the largest complete one fitting within the GMOS frame boundary) and within the photometric limits $i' < 25.4, 0.6 < (g' - i') < 1.4$. This sample is subdivided into 30° sectors and plotted against azimuthal angle θ of the sector, as shown in Figure 5. The two sectors containing the center of NGC 3309 and the guide probe shadow are shown as open symbols in Fig. 5 and are ignored.

It is evident that there is no strong trace of ellipticity in the residuals about the mean level of $\simeq 275$ objects per sector after background subtraction. Although there are sector-to-sector differences larger than the internal statistical uncertainties, they cannot easily be made to match an approximate double-cosine curve that would be the mark of a modestly elliptical distribution (McLaughlin et al. 1994, 1995). The integrated halo light of NGC 3311 has a small but definite ellipticity of $\epsilon = 0.2$ and major axis at $\simeq 30^\circ/210^\circ$ (Disney & Wall 1977; Vasterberg et al. 1991). If the formation of the GCS is closely associated with the galaxy halo, we should expect no large differences in their intrinsic shapes and orientations. Contrarily, a dramatic difference in the GCS shape or orientation relative to the halo light would be a signal of a more fundamental difference in the GCS formation era or its internal dynamical evolution.

We have carried out a solution for ϵ and θ_p with our GCS data, using the formalism of McLaughlin et al. (1994, 1995). They show that for an intrinsically ellipti-

cal distribution of points sampled in *circular* annuli, the observed number density is

$$\sigma(r, \theta) = \sigma_b + \sigma_0 r^{-\alpha} [\cos^2(\theta - \theta_p) + (1 - \epsilon)^{-2} \sin^2(\theta - \theta_p)]^{-\alpha/2} \quad (8)$$

where the radial falloff is modelled as a simple power law of exponent α . Here, $\theta_p \pm 180^\circ$ denotes the position angle of the major axis at which $\sigma(r, \theta)$ reaches its maximum value. For NGC 3311, we have $\alpha \simeq 1.2$ (for the Hubble profile fit described above, we found $\alpha = 2.0$, but if we remove the core-radius parameter c , we require a flatter overall power law to match the whole profile adequately). We then vary the assumed ϵ and θ_p till the residuals about this model are minimized.

The best-fit solution we find is for $\epsilon = 0.07(+0.11, -0.07)$ and $\theta_p = 90^\circ \pm 50^\circ$, shown as the solid curve in Fig. 5. The corresponding major axis line is thus $90^\circ/270^\circ \pm 50^\circ$. (In Fig. 3, the major axis would run vertically.) The best-fit solution is weakly determined with a shallow minimum at $\chi_\nu = 1.95$, and indeed solutions with $\epsilon \simeq 0$ are scarcely worse than this one. Our deduced ellipticity is lower than for the integrated light, and our solution for θ_p falls $\simeq 60^\circ$ eastward of the integrated halo light, though its uncertainty is large enough that there is no formal disagreement. In short, we appear to be confronted with no difficulties by assuming first-order circular symmetry.

For comparison, we show one of the solutions by McLaughlin et al. (1995) as the dashed line in Fig. 5; this clearly does not match our solution very well. McLaughlin et al. (1995) performed solutions for two different magnitude ranges ($T_1 \leq 23$, $T_1 \leq 24$) and for the more slightly more restricted radial range $0'.89 < r < 2'.22$. For $T_1 \leq 23$, they found $\epsilon = 0.32 \pm 0.05$, $\theta_p = 145^\circ$, while for $T_1 \leq 24$ they found $\epsilon \simeq 0.3$, $\theta_p = 190^\circ$ (this latter one is shown in our Fig. 5). They comment that “the uncertainty in θ_p is at least $\pm 40^\circ$ ”.

Both of the McLaughlin et al. solutions differ from ours; we find a distinctly smaller ellipticity and a position angle between their two solutions (although, again, it is not clear that any genuine formal disagreement exists). To attempt to trace down causes for the evident differences, we rebinned our data to magnitude ranges corresponding more closely to theirs, and also restricted to exactly the same radial range as they used. For these numerical trials we also included objects at all colors, as they did. For our objects brighter than $i' = 23$, we find $\epsilon = 0.34 \pm 0.15$ and $\theta_p \simeq 110^\circ/290^\circ$. For a slightly deeper cut down to $i' = 24$, we find $\epsilon = 0.10 \pm 0.07$ and $\theta_p \simeq 75^\circ/255^\circ$. Interestingly, the best-fit position angles of our two subsamples bracket our best solution from the large, ‘best’ dataset ($i' < 25.4$ and color-selected), but restricting the sample much more severely to the brightest objects tends to lead to a larger ϵ , as found by McLaughlin et al. Without being able to offer definitive reasons for the disagreement between these two studies, we suggest that the earlier GCS result was likely to have been compromised by the combination of small-number statistics, and especially by much larger relative field contamination (since the dominant source of field contamination is faint, small background galaxies which have clumpy space distributions, they are quite able to bias our solutions for the spatial distribution if they contribute a high fraction of the total sample). In the present data,

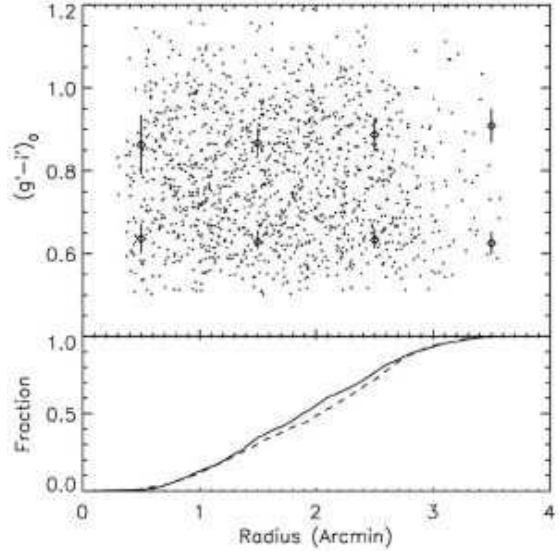


FIG. 6.— *Upper panel*: Color index $(g' - i')_0$ of globular clusters in our GMOS field, plotted as a function of radial distance from NGC 3311. All objects brighter than $i = 24.0$ are included here. The overlaid diamonds indicate the RMIX fits for the blue and red peaks of the distribution. *Lower panel*: Cumulative radial distributions of the metal-poor clusters (dashed line) and metal-rich clusters (solid line). The lower-metallicity clusters are slightly more extended spatially than the metal-richer ones, but not significantly so.

we have been able to reject non-GC objects more completely by color and morphology than in the older study.

The most intriguing feature of the azimuthal distribution is the residual difference between the GC system ($\epsilon \sim 0.1$, $\theta_p \sim 90^\circ$) and the halo *light* ($\epsilon \sim 0.2$, $\theta_p \sim 30^\circ$). Unfortunately, we are not yet in a position to place heavy significance on this, simply because the solution for the best-fit position angle is extremely uncertain if the ellipticity is very small. If the difference is verified with deeper and cleaner samples, it will, perhaps, be a tantalizing hint that the GC accretion or destruction histories differed in second-order ways from the field stars.

4.3. Radial Color Distribution

With the knowledge that the vast majority of GCs in this field belong to NGC 3311, we can also investigate their color distribution as a function of galactocentric distance. In many GCSs within large ellipticals, a color gradient can be found in the sense that the mean color of the GCs (averaging together both the red and blue ones) conventionally decreases with increasing R_{gc} . However, beginning especially with the key work of Geisler et al. (1996) on NGC 4472, it became clear that (in Geisler et al.’s concise wording) “most of this gradient appears to be due to the varying radial concentrations of the two populations”. That is, the metal-poor, blue GC population is less centrally concentrated than the metal-richer population and thus contributes a higher proportion of clusters at larger radius, generating an overall declining metallicity gradient in the GC population as a whole. Notably, each of the two metallicity components shows little or no color (metallicity) gradient of its own. Very much the same conclusion had already become clear long ago (albeit with a much smaller sample of GCs than can be found in giant ellipticals) for the Milky Way GCS (Zinn 1985).

In Figure 6 we show the color indices for the objects in

the NGC 3311 field (in order to minimize field contamination, we restrict the sample to the 1360 objects brighter than $i' = 24.0$). A broad range in color is present at all radii, but no strong radial gradient in color is evident for either the red or blue subpopulations, a similar result to other galaxies. In order to determine whether there was a trend in color versus radius, we binned the clusters in radius and performed a fit using RMIX (a fitting code discussed in detail in section 6). The locations of the red and blue peaks are shown as diamonds in Figure 6. A comparison between the cumulative distributions of the red and blue clusters (shown in the lower panel of the Figure) indicates that any difference has weak significance, at least within the regions our data are sampling. Unfortunately, the field size we sample reaches a maximum $R_{gc} \sim 50$ kpc, which is not large enough to test either the true spatial extent of the system or what happens to the color distribution near its outskirts (recall, for example, that the M87 GCS extends detectably outward to at least $R_{gc} \simeq 100$ kpc; see Tamura et al. (2006)).

4.4. Luminosity Function

Deep imaging from galaxies of all types now shows that the luminosity distribution of their GCs follows a roughly universal shape that has most often been approximated by a Gaussian distribution in number of GCs per unit magnitude (e.g. Harris 2001; Kundu & Whitmore 2001a,b; Larsen et al. 2001; Jordán et al. 2007, among many others). For giant galaxies, the turnover or peak frequency of the GCLF is consistently near $M_V^0 = -7.4 \pm 0.2$ (Harris 2001) while the intrinsic dispersion is in the range $\sigma = 1.3 - 1.5$ (see particularly Jordán et al. 2007, for an extensive analysis of the correlation of the turnover and dispersion with host galaxy luminosity, although it is worth noting that the only cD-type galaxy included in their data is M87).

Ideally, a determination of the GCLF for our target NGC 3311 would best be done by taking the LF of an adjacent “control field”, observed under identical conditions, and subtracting it from the LF of the objects in our 5:5-wide central field. Lacking this, a second-best alternative is to use the outer parts of our GMOS field as a “background”. In fact, much of the outer zone is still populated by GCs, and so by defining it as background we will partially subtract some of the GC population as well as the true background. However, as long as no large changes in the GCLF with radius exist, the residual GCLF we obtain this way will be systematically correct even if a bit oversubtracted.

An inevitable limitation of using the outer parts of the image field to define the background level is that the background estimate σ_b is much more uncertain numerically than if we had a large, remote control field to work with. We divide our field into two regions: an inner annulus of inner radius r_0 , outer radius r_1 , and area A_{in} ; and an outer zone of inner radius r_1 and outer boundary set by the edge of the frame, and area A_{out} . We set r_0 to be the innermost radius at which the photometry is still highly complete to the magnitude limit of interest ($i' \simeq 26$). The only significant free parameter we have to define these two zones is the mid-radius r_1 . The residual GC population within A_{in} after background subtraction

will clearly be

$$N_r = N_{in} - (A_{in}/A_{out})N_{out} \quad (9)$$

where, by hypothesis, the background σ_b is constant across the field and subtracts cleanly out after the area normalization. We would like to choose the midpoint r_1 in such a way as to minimize the relative uncertainty in $\sigma(N_r)/N_r$. If r_1 is too large, then N_r will be large, but the area normalization factor (A_{in}/A_{out}) will blow up and the background correction becomes extremely uncertain. But if r_1 is too small, then so is N_{in} , and again the relative uncertainty in the residual population becomes large.

To fix r_1 , we adopted the radial profile parameters described above for the GC system (the best-fit Hubble profile plus the background level $\sigma_b = 18$ arcmin⁻²). The inner radius r_0 is set at 0'.5. We then calculated the resulting relative uncertainty $\sigma(N_r)/N_r$ as a function of r_1 , where we let r_1 vary from just slightly larger than r_0 out to almost the borders of the field. The optimum r_1 turns out to be roughly halfway from the center of NGC 3311 to the edge of the field, given the geometry of this system, but the relative uncertainty goes through a very shallow minimum near this point and the precise choice is not critical. For the following discussion, we use $r_1 = 2'.5$. The “background” region is defined to be everything beyond that radius, though not including the vignetted regions in the outskirts. In each zone we count all objects within the broad color range $0.2 < (g' - i') < 1.4$, and also correct the raw numbers of objects in each bin for photometric incompleteness $f = f_{i'} \cdot f_{g'}$ with the completeness function parameters derived above.

The results are in Figure 7, shown in $\Delta i' = 0.2$ -mag bins. For $i' > 26.5$, the net completeness f falls below 0.5 and the LF becomes considerably more uncertain (note the rapid growth of the internal error bars). This level is also very near the *predicted* magnitude of the GCLF turnover point for a normal giant or supergiant elliptical galaxy. For $M_V^0 \simeq -7.4$ and $\langle V - I \rangle_0 = 1.0$, we expect $M_I^0 \simeq -8.4$ or $I^0 = 25.22$ adding the distance modulus $(m - M)_0 = 33.62$. To convert I to i' , we use the mean difference $\langle i' - I \rangle = 0.28 \pm 0.02$ determined directly within our field from 12 of the brightest GCs (see Wehner & Harris 2007). Finally adding the foreground extinction $A_I \simeq A_{i'} = 0.15$, we have $i'(\text{turnover}) \simeq 25.65$. A Gaussian curve with that peak magnitude and with $\sigma = 1.5$ mag is shown superimposed on the observed GCLF in Fig. 7. Encouragingly, the raw LF of all objects within the inner zone (shown as the open circles) has the same peak to within ~ 0.1 mag even without background subtraction.

The Gaussian curve shown in Fig. 7 is not intended to represent a rigorous derivation of the observed turnover point or dispersion; we use it only to show that the standard values provide an entirely plausible description of the data for NGC 3311. That is, the GCLF in this cD galaxy gives no indication of being unusual. Our photometry does not reach far enough past the turnover to permit any kind of useful test of more sophisticated numerical models, such as the asymmetric Schechter-like function explored in depth by Jordán et al. (2007) from the Virgo cluster survey. However, in a broader sense our data clearly show that imaging with ground-based 8m-

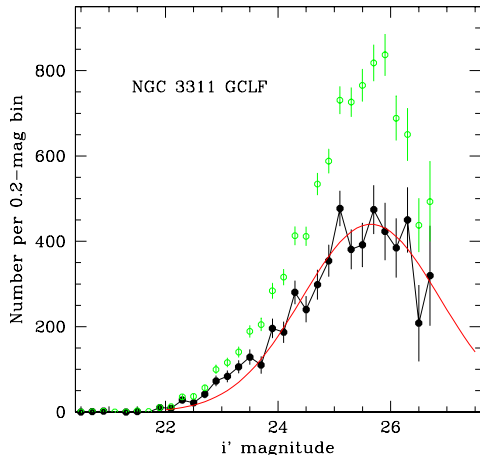


FIG. 7.— Luminosity function for the globular clusters in NGC 3311. The *open circles* with errorbars show the numbers of objects within the radial range $0.5 < r < 2.5$. The connected *solid dots* with errorbars are the totals after approximate background subtraction, where the GMOS image region outside the circle $r > 2.5$ is used to define the background. The red solid line is a Gaussian LF with peak at $i' = 25.65$ (corresponding to $M_V \simeq -7.4$) and with standard deviation $\sigma_{i'} = 1.5$.

class telescopes is capable of penetrating deep into the globular cluster populations of galaxies in the 50-Mpc distance range and even beyond.

Recent interest has followed the possibility that the GCLFs may differ between the redder and bluer metallicity groups of clusters. If the underlying *mass* distributions of both types of clusters are similar, then the GCLF turnover magnitude should differ between photometric bandpasses by typically ~ 0.2 mag purely because of differential bolometric correction (Ashman et al. 1995). Larger differences between the red and blue GCLFs (or ones in the opposite sense expected from bolometric corrections) may be indicators of genuine differences in their mass distributions. In an HST-based survey of several nearby ellipticals, Larsen et al. (2001) found a mean difference $\Delta M_V = 0.4$ mag in the sense that the blue GCLF peak was brighter, though large and uncertain differences show up from one system to another. They conclude that it is unclear whether any true underlying mass differences are required to explain this mean difference.

NGC 3311 has large numbers of both red and blue clusters, and using the same numerical technique as described above, we determined their GCLFs separately. “Blue”, metal-poor clusters are defined to lie within the color range $0.2 < (g' - i')_0 < 0.8$ and “red”, metal-rich clusters within $0.8 < (g' - i')_0 < 1.4$. The results are shown in Figure 8, where we display only the residual LFs and not the raw numbers before background subtraction. The blue population falls close to the same roughly-Gaussian curve describing the system as a whole. For the red population, the small excess of very luminous clusters ($i' < 23$) is evident, but the most striking difference is in the range $i' = 25 - 26$, where a noticeable dip is seen just around the nominal turnover point. We are, however, reluctant to conclude that this effect is real given the uncertainties in the background correction and the determination of residuals. A standard Kolmogorov-

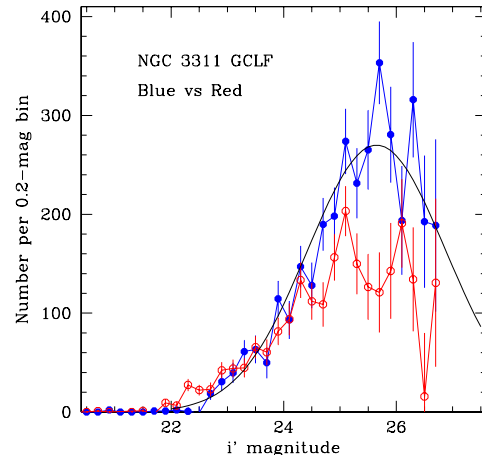


FIG. 8.— Luminosity function for the globular clusters in NGC 3311, plotted separately for the blue and red GC sequences. The *open circles* with errorbars show the redder clusters lying in the color range $0.8 < (g' - i')_0 < 1.4$, while the *solid dots* with errorbars show the bluer clusters in the color range $0.2 < (g' - i')_0 < 0.8$. Both sets of points have been background-subtracted as described in the previous figure. The solid line is a Gaussian LF with the same mean and standard deviation as in the previous figure, matching the entire GCLF over all colors.

Smirnov two-sample test shows that the two LFs differ over the range $i < 26$ at more than 99% confidence, but the strongest statement we feel is justified from the present data is that the bright-end slope for the red clusters is somewhat flatter than for the blue ones. A better control field, and perhaps even better selection of GCs versus field contamination, will be needed to carry this discussion any further.

4.5. Specific Frequencies

Finally, we use the radial distributions we have derived for NGC 3311 and NGC 3309 to estimate the total cluster populations around each one, and thus their specific frequencies. We use the best-fit Sersic profile parameters given above, and integrate them outward to large enough radius r_{max} that the GC population totals converge. For NGC 3309, the particular choice of r_{max} is quite unimportant, since its profile is steep and negligible numbers of GCs are added for $r \gtrsim 3'$. However, the much more extended profile for NGC 3311 requires us to integrate outward to $r_{max} \simeq 9'$ or about 140 kpc, beyond which the Sersic model profile adds negligible numbers of GCs. This large radius is, however, quite consistent with the existing surface photometry (Richter et al. 1982; Vasterberg et al. 1991) which shows that NGC 3311 extends detectably to $r \sim 150$ kpc. With these parameters in mind, we find total GC populations brighter than $i' = 25.4$ equal to $N_{3311} = 7440$ and $N_{3309} = 165$.

Evaluating the actual population totals requires correcting for the magnitude limit and the fraction of GCs fainter than that limit. Assuming a Gaussian-like GCLF as discussed in the previous section, with a turnover point at $M_V \simeq -7.4 \pm 0.1$ and standard deviation $\sigma_V \simeq 1.5$, then $i' = 25.4$ is 0.25 ± 0.1 mag or 0.17σ brighter than the turnover point. This part of the GCLF includes a

fraction (0.45 ± 0.04) of the total population. We therefore estimate the total GC population for NGC 3311 as $N_t \simeq 16500 \pm 2000$, where the main uncertainty is the necessary extrapolation to large radius.

For NGC 3309 we find $N_t = 364 \pm 210$; here, the relatively large internal error is dominated instead by the large uncertainty in the ratio (σ_{e2}/σ_{e1}) = 0.080 ± 0.046 for the two-function fit described above. In this case our calculation may be a slight underestimate, not because of what may be present at larger radius, but because of the uncertain *inward* extrapolation into the central $\sim 20''$. Its GCS core radius is both smaller and considerably more uncertain (by a factor of two; see above), and our profile integration may not have accounted for a significant part of the total. The HST photometry to be discussed in the next section verifies that more GCs are present in its core.

Their specific frequencies can be determined once we know their total luminosities. Vasterberg et al. (1991) measure integrated magnitudes $V_T = 11.04$ for NGC 3311 and 11.94 for NGC 3309 (we have reconstructed these numbers from their Table 5 and their adopted distance and reddening). With our adopted $(m - M)_V = 33.88$, their luminosities are $M_V^T(N3311) = -22.8$ and $M_V^T(N3309) = -21.9$. The (global) specific frequency of the NGC 3311 GCS is then $S_N = N_t \cdot 10^{0.4(15 - M_V^T)} = 12.5 \pm 1.5$, and for NGC 3309 $S_N = 0.63 \pm 0.36$. It should be noted, however, that these total magnitudes are extrapolations to large radius of the $r^{1/4}$ profiles that were found to fit the inner regions, and for NGC 3311 at least a part of the excess cD envelope light would be missed. Vasterberg et al. estimate that it should be made $\simeq 0.4$ mag brighter, which would give $M_V^T(N3311) = -23.2$. If this adjustment is applied, its specific frequency would be lowered to $S_N = 8.7 \pm 1.0$. However, it is not clear that the luminosity should be increased without also making a similar adjustment to the total cluster population, since we might have missed some of the GCs by using only the extrapolation from the inner profile. For the present time, and pending a more quantitative measurement of the cD envelope light, we use $S_N \simeq 12$, while $S_N \sim 9$ should be considered an extreme lower limit.

By contrast, NGC 3309 has a remarkably low deduced cluster population, even with the uncertainties about the core population. Giant E galaxies in rich cluster environments with $S_N \lesssim 1$ are rare, but not unprecedented. For example, Baum et al. (1995) found $S_N < 1$ for one of the Coma cluster giants NGC 4881. It is tempting to imagine that an object like NGC 3309 might have had much of its original GCS removed by tidal stripping in passages through the cluster core. Regardless of its history, it is clear that today, NGC 3311 completely dominates the GCS population in the core Hydra field, in equal measure because of its higher total luminosity and its higher intrinsic S_N . The wide ranges of S_N that we find among these giant and structurally simple E galaxies are still not fully understood and may require combinations of formation conditions, later dynamical evolution in the potential field of their cluster, and accounting for the presence or absence of hot halo gas (e.g. Harris 2001; McLaughlin 1999).

As a final test of the relative GC populations of the two galaxies, we ran another solution for Eq. 4 where we

imposed the *assumption* that the total number of GCs in each galaxy was in proportion to the luminosity of the galaxy; that is, they have the same S_N . This requirement converts to $N_{GC}(3311)/N_{GC}(3309) \simeq 2.5$. The best-fit solution gave $\chi_\nu^2(\min) \simeq 2.8$, worse than our optimum solutions described above ($\chi_\nu^2 = 2.0$) though not dramatically so. The implication is simply that the parameters for the NGC 3309 system are poorly constrained within broad limits, a statement that is already reflected in the large uncertainty on its deduced best-fit cluster population.

NGC 3311 clearly holds one of the very largest globular cluster systems in the local universe, rivalling that of the classic high- S_N prototype M87 which has $N_t \simeq 13000$ and $S_N \simeq 13$ (McLaughlin et al. 1994; Tamura et al. 2006). The NGC 3311 GCS is spatially very extended, marked by a huge core radius $c = 94'' = 24$ kpc or effective radius $r_e = 177'' = 45$ kpc also comparable to that of the GCS in M87 (McLaughlin 1999).

5. WFPC2 PHOTOMETRY

To gain additional insight into the relative properties of the GCSs around NGC 3309 and 3311, we employed imaging in (V, I) from the HST WFPC2 camera that was available in the HST Archive. Two WFPC2 fields were taken as part of GO program 6554 (PI Brodie) in Cycle 6, each with total exposures of 3700 sec in $F555W$ and 3800 sec in $F814W$. In one field, the PC1 chip was centered on NGC 3311, and in the second field, the PC1 chip was centered on NGC 3309. Photometry of the NGC 3311-centered field was published in Brodie et al. (2000), but to our knowledge, no measurements from the NGC 3309 imaging have been published.

We have carried out photometry on both of these WFPC2 fields with *daophot* in the same manner as described above. A typical globular cluster with a half-light radius of ~ 3 pc will, at the distance of Hydra, have an intrinsic FWHM $< 0''.03$, making it entirely feasible to perform PSF-fitting photometry with the WFPC2 resolution of $0''.1$. For each of the four WFPC2 CCDs, we registered and co-added the individual exposures downloaded from the HST Archive, and performed the usual sequence of *daophot* FIND/PHOT/PSF/ALLSTAR. Detected objects on the V and I frames that matched locations within 2 pixels, and with ALLSTAR goodness-of-fit $\chi_{V,I} < 2.0$, were kept for the final data list. Calibrations followed the normal prescriptions in Holtzman et al. (1995), based on $0''.5$ aperture photometry of the brightest objects. The data for the four CCDs were then combined to yield the results shown in Figures 9 and 10. The photometric limit near $I \simeq 25$ or $i' \simeq 25.3$ is about half a magnitude shallower than for our GMOS data.

Our PSF-based photometry for NGC 3311 has generated a slightly tighter CMD than the work of Brodie et al. (2000) (who used only aperture photometry), but no major differences. Though the $(V - I)$ color index is notoriously insensitive to metallicity (with an intrinsic difference of only 0.2 mag between the red and blue sequences), a clear trace of bimodality can be seen (also see Brodie et al. 2000). Notably, on the red side at $\langle V - I \rangle \simeq 1.2$, the upward extension of the GC sequence into the high-mass UCD-like range that is more evident in our more comprehensive GMOS photometry (Wehner & Harris 2007) can also be seen here. In gen-

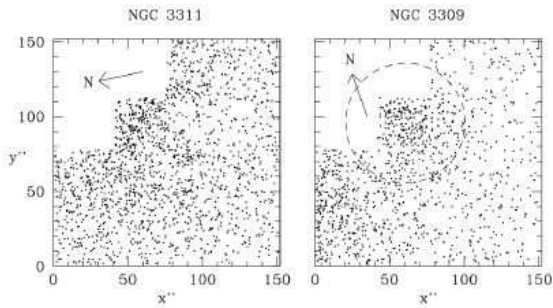


FIG. 9.— WFPC2 fields in the Hydra core. The panel on the left shows the data for the field in which the PC1 chip is centered on NGC 3311, while the right panel shows the field centered on NGC 3309. All measured objects brighter than $I = 25.0$ are plotted. The xy positions on the frames are plotted in arcseconds. Notice that the orientations of the two fields are different: for NGC 3311, North is 109.8° counterclockwise from vertical, and for NGC 3309, North is 19.7° counterclockwise from vertical. Within the “NGC 3309” field, the center of NGC 3311 lies to the lower left; notice the increase in numbers of measured points there.

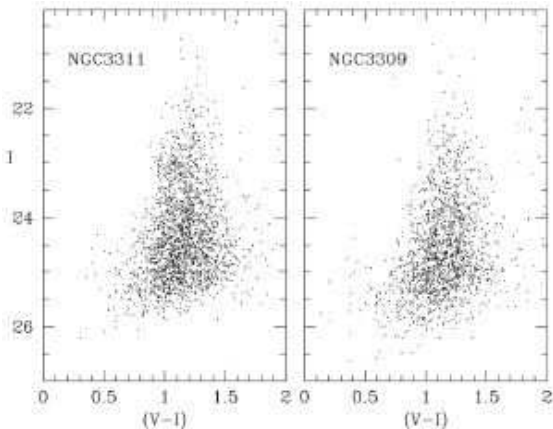


FIG. 10.— Photometry for the measured starlike objects in the two WFPC2 fields shown in the previous figure.

eral, both CMDs in Fig. 10 resemble each other closely.

In the xy plots of Fig. 9, we see the “NGC 3309 problem” once again. In the so-called NGC 3309 field, a population of GCs is present on and near the PC1 chip centered on 3309; but the presence of the NGC 3311 GCS is extensive everywhere over the field (note particularly the lower left region of the xy plot where the increase in GC number density toward the center of NGC 3311 is particularly obvious). Even though the exposures were intended for study of the NGC 3309 system, the majority of detected objects in it actually belong to NGC 3311. From our quantitative double-profile solutions in the previous section, it can easily be shown that for any location further than $40''$ from the center of NGC 3309, the GCS of NGC 3309 contributes less than 10% of the GC counts. This transition boundary beyond which the NGC 3309 system becomes unimportant is indicated by the dashed circle in Fig. 9. The CMD for this inner zone is shown in Figure 11, where we have included the ≈ 360 detected objects within an even smaller radius of $30''$. In this diagram, which gives us our best look at the GC population of NGC 3309 alone, the high-luminosity end of the CMD is not as well populated as in the NGC 3311 GCS (perhaps a simple result of small-number statistics), but otherwise there are no striking differences to note.

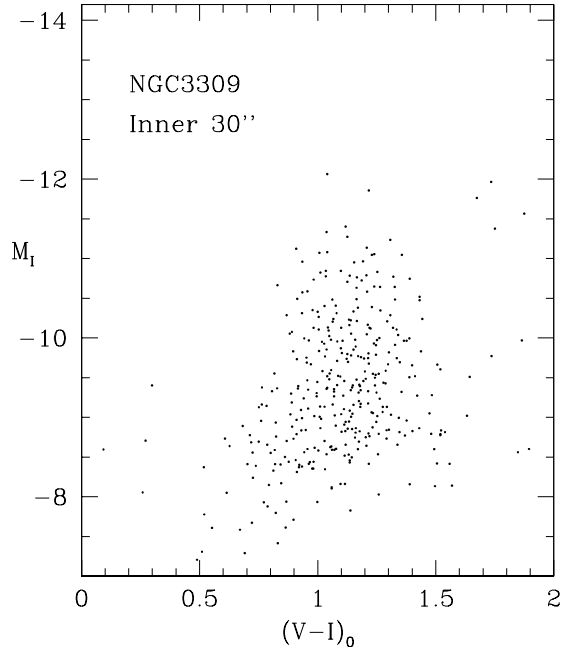


FIG. 11.— Photometry for measured objects within $30''$ of the center of NGC 3309.

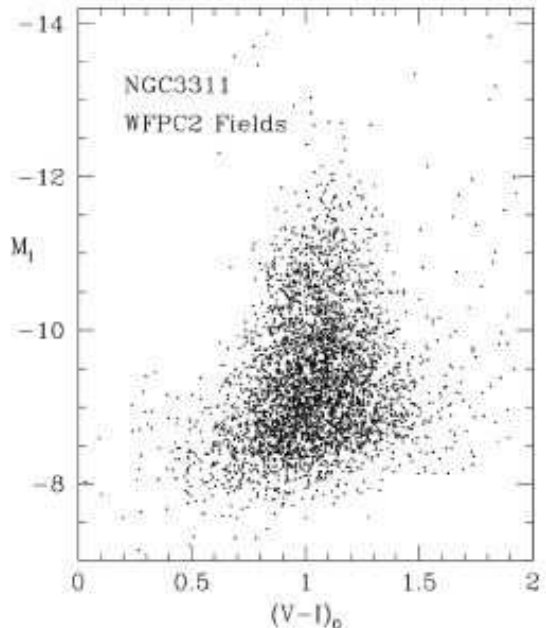


FIG. 12.— Color-magnitude data for both WFPC2 fields combined, excluding any objects within $40''$ of the center of NGC 3309 (within the dashed circle in Fig. 9). This CMD is completely dominated by GCs belonging to NGC 3311.

In Figure 12, we have combined the photometry from both WFPC2 fields, excluding only the points within the $40''$ zone around NGC 3309. This CMD, dominated by NGC 3311, will be analyzed below simultaneously with the GMOS data, for bimodality characteristics of the metallicity distribution.

6. THE METALLICITY DISTRIBUTION AND ANALYSIS OF THE BIMODALITY

A primary goal of our study was to investigate the multimodal structure of the GC color and metallicity distri-

bution, and in particular to find out whether or not the blue GC sequence would reveal the same mass-metallicity relation as in other large galaxies. Having measured several other properties of the system, including the fact that the GC population in our target field is dominated by NGC 3311, we now discuss the color distribution.

The histogram of colors ($g' - i'$) over any selected magnitude range drawn from Fig. 2 indicates immediately that the color distribution is broad and not well fit, for example, by a single Gaussian-type curve (also found by Brodie et al. 2000, from their WFPC2 photometry). A better description of the system is by conventional “blue” and “red” sequences whose color distributions partially overlap. The bright-end extension of the red sequence in particular reaches upward into the UCD luminosity range (Wehner & Harris 2007). We therefore experimented with bimodal fits in a variety of ways, to help define the mean colors and dispersions of these two components.

To carry out quantitative fits to the color distribution, we employed the statistical code RMIX (MacDonald 2007), a library written with the statistics programming language, R. This package allows the user to fit data with various functional shapes and to set constraints on them at a range of possible levels. RMIX does not restrict the fitting to unimodal or bimodal forms; the number of components adopted to fit the data is user-defined, as are the functional forms of the curve (e.g. Gaussian, Poisson, binomial) and the starting values for the modes and dispersions of each component (e.g. the peak and standard deviation, in the Gaussian case). In addition, the dispersions can be constrained to be equal (homoscedastic) or allowed to differ between components (heteroscedastic), as appropriate. The numerical values of the dispersions can also be set to previously determined numbers, or can be determined by the fit, in any combination between the components.⁴

The KMM software (McLachlan & Basford 1987; Ashman et al. 1994) is a well known code frequently used in the literature for bimodal fits to GCS color distributions (see, e.g. Larsen et al. 2001; Mieske et al. 2006, among many such examples). We have experimented with both KMM and RMIX in this study. Both give quite similar results for a given dataset, but we find that the RMIX package offers more flexibility in its choice of fitting functions as well as better flexibility in managing user-defined constraints on the fitting parameters. It is also more robust, successfully converging on multimodal fits in small-sample cases where KMM would not run. We recommend RMIX as an attractive and statistically rigorous alternative.

Figure 13 shows some of our results for four different magnitude subsets of our (g', i') data. For each magnitude bin shown, we fit a pair of Gaussian curves to the ($g' - i'$) histogram. Reasonable initial guesses for the peaks and dispersions were provided, and the component means and dispersions were determined by the fit itself with the condition that the dispersions of the two Gaussians were required to be the same. The re-

TABLE 2
RMIX FITS TO THE COLOR DISTRIBUTION

i' Range	f(blue,red)	$\langle g' - i' \rangle_b$	$\langle g' - i' \rangle_r$	σ_b, σ_r	χ^2_ν
22 – 23	(0.48,0.52)	0.850 ± 0.015	1.073 ± 0.014	0.082 ± 0.008	1.38
23 – 24	(0.64,0.36)	0.840 ± 0.010	1.095 ± 0.013	0.108 ± 0.006	2.34
24 – 25	(0.62,0.38)	0.778 ± 0.015	1.082 ± 0.020	0.172 ± 0.008	1.35
25 – 26	(0.72,0.28)	0.705 ± 0.013	1.077 ± 0.021	0.186 ± 0.007	2.11

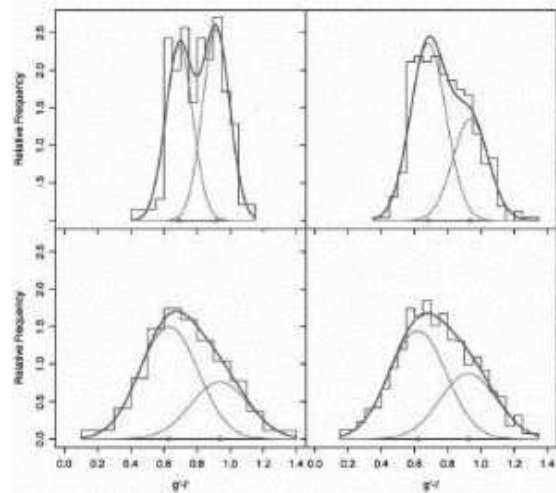


FIG. 13.— Color distribution for the globular cluster population in NGC 3311, as a function of magnitude. Number of GCs per unit ($g' - i'$)₀ interval is plotted for four different luminosity bins as listed in Table 2. The interval $i' = 22 - 23$ is at upper left, 23 – 24 at upper right, 24 – 25 at lower left, and 25 – 26 at lower right. In each panel, the bimodal Gaussian fit as determined by the RMIX code is shown overlapped on the histogram of the data. The two individual Gaussians matching the metal-poor and metal-rich components are shown by the red lines, while the green envelope is the direct sum of the two components. Small filled triangles on the x-axis of each plot mark the mean color (Gaussian peak position) of each component. Note that the metal-poor component becomes progressively redder at higher luminosity, while no significant change occurs for the metal-rich component.

sults are summarized in Table 2. Here, the first column gives the magnitude range; column 2 the deduced proportions of the blue and red components; columns 3 and 4 the mean colors of the blue and red sequences; column 5 the standard deviation of each sequence; and the last column the goodness of fit. Bimodal fits are strongly preferred over unimodal ones for the two brighter bins. In the two faintest bins the overlap between the red and blue components increases because of the combination of field contamination and larger photometric uncertainty, and the distinction between bimodal and unimodal fits becomes less clear.

In Fig. 13, one can see that the peak of the bluer component shifts closer to the red component at brighter magnitudes, suggesting the presence of a mass-metallicity trend for at least one of the modes. To explore this further, we separated the GC population into blue and red halves by taking the intervals $0.3 < (g' - i')_0 < 0.8$ (blue) and $0.8 < (g' - i')_0 < 1.2$ (red), and then calculating the mean color of each mode in half-magnitude bins. The combined results can be seen in Figure 14. Linear least-squares fits over the en-

⁴ The complete code, available for a variety of platforms, is publicly available from Peter MacDonald’s website at <http://www.math.mcmaster.ca/peter/mix/mix.html>. The same site gives links to an extensive bibliography with further examples of its use.

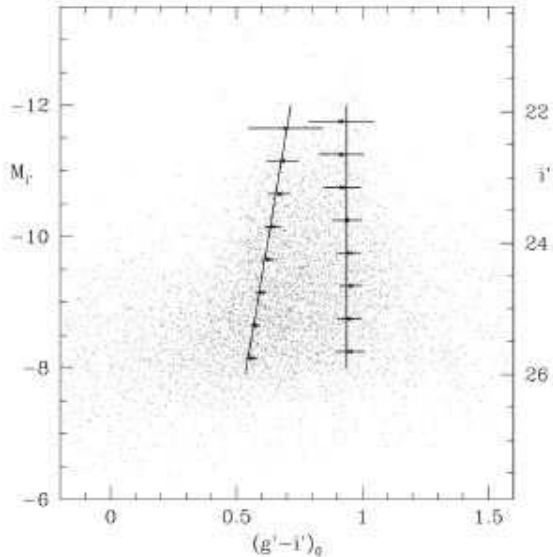


FIG. 14.— Color-magnitude diagram for the NGC 3311 globular cluster system, plotted as absolute magnitude $M_{i'}$ versus dereddened color. Mean points for the blue and red globular cluster sequences are overplotted, derived as described in the text. The error bars on each point are the one-sigma uncertainties in $(g' - i')_0$. The best-fit mean lines determined by linear least squares are drawn through each sequence. For the blue sequence, the slope is $\Delta(g' - i')/\Delta i' = 0.044 \pm 0.011$, corresponding to a heavy-element abundance scaling with cluster mass of $Z \sim M^{0.6}$. The red GC sequence shows no net change in color with magnitude, and is assumed for the purposes of this plot (see text and previous figure) to be at a fixed color of $(g' - i')_0 = 0.94$.

tire GC luminosity range $22 < i' < 26$, weighted by $1/\sigma^2$ where the uncertainty of each mean color is σ , give $\Delta(g' - i')/\Delta i' = 0.044 \pm 0.011$ for the blue sequence with a correlation coefficient of the fit equal to 0.995, indicating that a MMR is present at high significance. For the red sequence, $\Delta(g' - i')/\Delta i' = 0.012 \pm 0.021$, indicating no significant trend with magnitude. In Fig. 14 we show it simply as an average $(g' - i')_{0,red} = 0.94$.

Field contamination at magnitude levels $i' \lesssim 25$ is unimportant, so at these relatively bright levels in the color-magnitude diagram the existence of an MMR seems secure. Fainter than this, however, contamination becomes progressively worse and is likely to affect these simple linear fits to uncertain degrees. Thus for the fainter parts of the sequences (roughly, $M_{i'} \gtrsim -9.5$) we cannot test with any confidence whether or not the blue sequence really does continue to get “bluer” as it goes down. In Harris et al. (2006), we claimed that the blue sequence became approximately vertical (that is, no MMR) for luminosity levels $M_I \gtrsim -9.5$. That claim was based on bimodal fits to the color distributions in finely spaced magnitude bins for the eight BCGs studied there; however, in most of those galaxies the issue of faint-end field contamination is also a concern just as it is here. For NGC 4594, Spitler et al. (2006) suggest that the blue-sequence MMR continues downward roughly linearly to fainter luminosities, though their two faintest blue-sequence bins are not distinguishably different in mean color, and their conclusion of the same MMR at all luminosities is in part forced by their assumption of a linear fit. To quote them directly, “Indeed, whether the faintest bins follow the trends established by the brighter points is indeterminate.” For our NGC 3311

data, removing the two faintest bins, where we expect the contamination to be most significant, as well as the top bin, which may be affected by the presence of Ultra Compact Dwarfs (Wehner & Harris 2007), yields a similar fit of $\Delta(g' - i')/\Delta i' = 0.040 \pm 0.011$. As such, the resulting slope does not appear to be driven by contamination in the faintest magnitude bins. Lastly, Mieske et al. (2006) use the combined GCS data for 79 Virgo galaxies to test for color trends by combining their target galaxies into four groups by luminosity. In their data, field contamination is much less of a concern because individual GCs were carefully selected by a series of morphological and photometric criteria. For the highest-luminosity galaxies (M87, M49, and M60; see their Figures 1 and 2) it can reasonably be claimed that the blue-sequence MMR continues roughly linearly over the entire luminosity range $-11 > M_{z'} > -7$. For the other groups containing a total of 76 galaxies from giants to dwarfs, the blue GC sequence clearly shows a color trend at bright levels but could reasonably be claimed to become nearly vertical for $M_{z'} \gtrsim -9$, corresponding roughly to $M_{i'} \gtrsim -8.5$.

At the present stage in this subject, we cannot yet say on the basis of the empirical evidence whether or not the blue-sequence MMR persists at all luminosity levels. More complete data allowing for accurate removal of field contamination will be needed to trace it out at the crucial faint levels. All studies to date agree, however, that a MMR exists for the blue clusters brighter than about $M_I \sim -9.5$, and that this seems to be a nearly universal phenomenon.

Comparing our MMR for NGC 3311 with those found previously for other large galaxies requires transformations between photometric systems, since H06 used $(B - I)$, whereas Mieske et al. (2006) and Strader et al. (2006) used $(g' - z')$. Ideally, we would like to convert $(g' - i')$ to either one of these other indices, but transformations based directly on observations of standard globular clusters (the Milky Way clusters, for example) do not yet exist. For the purposes of a preliminary comparison, we choose instead to transform the observed blue-sequence slope $\Delta(g' - i')$ into a metallicity scale $\Delta[\text{Fe}/\text{H}]$ through the use of models. Representative calculations of integrated colors for SSP systems are given by Maraston (2005) and Girardi et al. (2004). For the range with $[\text{m}/\text{H}] \lesssim -0.5$, these two sets of models agree well with each other and give $\Delta(g' - i')/\Delta[\text{m}/\text{H}] = 0.18 \pm 0.03$ for the metallicity regime we are concerned with, i.e. $[\text{m}/\text{H}] \lesssim -1.2$. Then, converting color index to metallicity, and magnitude to luminosity and hence mass, we find that the MMR for the blue sequence in NGC 3311 corresponds to a heavy-element abundance scaling with cluster mass $Z \sim M^{0.6 \pm 0.2}$. As we did in Wehner & Harris (2007), we assume that (M/L) does not change systematically with luminosity in order to convert L to M and thus derive the scaling. By comparison, H06 found a mean scaling $Z \sim M^{0.55}$ for their sample of eight giant galaxies. Mieske et al. (2006) found $Z \sim M^{0.48 \pm 0.08}$ for their Virgo galaxy sample. Our results for NGC 3311 are entirely consistent with the other studies within measurement uncertainties.

As an additional check of the $(g' - i')$ analysis, we perform the same kinds of bimodal Gaussian fits to the WFPC2 data in $(V - I)$. Here, the smaller size of the $(V - I)$ sample, and its lower sensitivity to metallicity, prevent

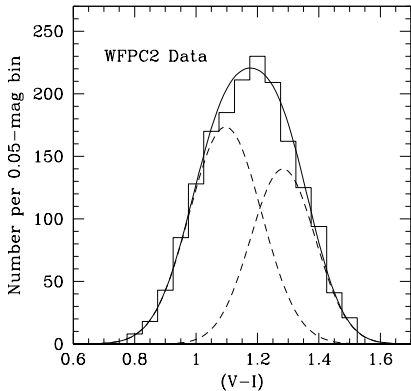


FIG. 15.— Color distribution for globular clusters in NGC 3311, from the WFPC2 $(V - I)$ photometry discussed in the text. No dereddening has been applied. The double-Gaussian bimodal fit to the data is shown, where the solid curve equals the sum of the two individual components shown in the dashed lines. The parameters for the two components are listed in the text.

us from tracing out mean color trends with magnitude with any confidence, so we use a color histogram defined from only a single magnitude range $21.5 < I < 24.5$ over which the field contamination and photometric scatter are minimized. As before, we exclude the region within $40''$ of NGC 3309.

The histogram of 1730 such objects is shown in Figure 15. We ran RMIX under similar assumptions as described above (two Gaussians, with means, dispersions, and proportions determined by the fit). For the blue, metal-poor component we find $\langle V - I \rangle = 1.10 \pm 0.07$, $\sigma_{V-I} = 0.12 \pm 0.02$, and proportion of the total population $p(blue) = 0.58 \pm 0.39$. For the red, metal-rich component, $\langle V - I \rangle = 1.28 \pm 0.07$, $\sigma_{V-I} = 0.11 \pm 0.02$, and $p(red) = 0.42 \pm 0.39$, with an overall $\chi_\nu = 1.22$. The relative proportions of the two components are quite uncertain – again, a direct result of the insensitivity of $V - I$ to metallicity and thus the heavy overlap between the two components – but agree nominally with the near-equal proportions we found from the $(g' - i')$ solutions (Fig. 13). For comparison purposes, we also tried a fit of a single Gaussian curve to the entire data: this yielded a best-fitting mean $\langle V - I \rangle = 1.175 \pm 0.004$ and dispersion $\sigma_{V-I} = 0.146 \pm 0.003$, with goodness-of-fit $\chi_\nu = 1.47$. The bimodal fit performs better at matching the data.

Although $(V - I)$ is less sensitive to metallicity, it has the advantage over the SDSS indices that its conversion to $[\text{Fe}/\text{H}]$ is more well determined. With $E_{V-I} = 0.11$, we have $\langle V - I \rangle_0(blue) = 0.99 \pm 0.07$ and $\langle V - I \rangle_0(red) = 1.17 \pm 0.07$. Adopting a conversion $(V - I)_0 = 0.16 [\text{Fe}/\text{H}] + 1.15$ (Harris et al. 2000; Barmby et al. 2000) based on calibration from the Milky Way and M31 clusters then gives $[\text{Fe}/\text{H}] \simeq -1.2$ for the blue sequence and $\simeq +0.2$ for the red sequence. These mean metallicities should be taken only as rough estimates, since the red-sequence mode in particular requires an extension of the conversion equations into a high-metallicity regime that the calibrating GCs in M31 and the Milky Way do not ad-

equately cover. However, the mean $(V - I)_0$ values themselves are close to what would be predicted from the established correlations with host galaxy luminosity (Larsen et al. 2001; Strader et al. 2004), namely

$$\langle V - I \rangle(blue) = -0.011M_V^T + 0.71, \quad (10)$$

$$\langle V - I \rangle(red) = -0.018M_V^T + 0.80 \quad (11)$$

For $M_V^T(NGC3311) = -22.8$ these relations predict $\langle V - I \rangle_0 = 0.96$ and 1.19 for the blue and red modes respectively, in good agreement with our observed mean colors. Supergiant ellipticals such as this one are the most logical places to search for GCs of super-Solar metallicity, although higher quality spectra than currently exist will be required to establish their abundances accurately.

7. SUMMARY

We have presented an extensive new photometric study of the large globular cluster system around NGC 3311, the central cD galaxy in the Hydra cluster. The relatively wide field and deep limiting magnitude of our data from the Gemini/GMOS camera has allowed us to analyze the GCS with a sample of several thousand globular clusters; our data reach to $i'(lim) \simeq 26.3$, just beyond the turnover point of the GC luminosity function. Among our findings are these:

- The classic metal-poor blue GC sequence and the metal-rich red sequence are both present at their expected colors, and with nearly equal populations. We show the color distributions both from our GMOS $(g' - i')$ photometry and from HST WFPC2 archival data in $(V - I)$.
- Bimodal fits to the complete color distribution, subdivided by magnitude, confirm that the blue sequence has the same correlation of progressively increasing metallicity with GC mass that was previously found in many other large galaxies; the correlation we find corresponds to a scaling of GC metallicity with mass of $Z \sim M^{0.6}$.
- By contrast, the red sequence shows no change of mean metallicity with mass, though it does extend upward to much higher than normal luminosity into the UCD-like range, strengthening the potential connections between massive GCs and UCDs.
- Confirming previous but much more preliminary investigations, we find that the GCS in NGC 3311 falls definitively into the “high specific frequency” category inhabited almost uniquely by supergiant ellipticals (cD’s or BCG’s) at the centers of rich clusters. NGC 3311 has an estimated total population of about 16,000 clusters and a specific frequency $S_N \simeq 12$.
- At the core of the Hydra cluster, another giant elliptical NGC 3309 is sitting projected just $100''$ from the cD NGC 3311. We use our database to solve simultaneously for the spatial structure and total GC populations of both galaxies at once. The results show that NGC 3309 contributes only a few percent of the GC population over the entire field,

and has an unusually (though not unprecedentedly) low value $S_N(N3309) = 0.6 \pm 0.4$. The central cD is completely dominant in the central Hydra region.

- The GC luminosity function, which we measure down to the “turnover” point at $M_I \simeq -8.4$, also has a normal structure relative to other giant ellipticals.

Additional observations that could make clear improvements to the understanding of the NGC 3311 system would include imaging with a still wider field (to establish a true “control” field for background measurement), and multicolor photometry with still more sensitive color indices to improve the definition of the metallicity distribution function. The resources held by this enormous and fascinating GC system are far from being

exhausted.

The authors would like to thank the anonymous referee for their helpful comments in improving this paper. This work is based on observations obtained at the Gemini Observatory, which is operated by the Association of Universities for Research in Astronomy, Inc., under a cooperative agreement with the NSF on behalf of the Gemini partnership: the National Science Foundation (United States), the Science and Technology Facilities Council (United Kingdom), the National Research Council (Canada), CONICYT (Chile), the Australian Research Council (Australia), CNPq (Brazil) and CONICET (Argentina). EMHW, WEH, and KAW thank the Natural Sciences and Engineering Research Council of Canada for financial support.

REFERENCES

- Ashman, K.M., Bird, C.M., & Zepf, S.E. 1994, *AJ*, 108, 2348
 Ashman, K.M., Conti, A., & Zepf, S.E. 1995, *AJ*, 110, 1164
 Baum, W.A., Hammergren, M., Groth, E.J., Ajhar, E.A., Lauer, T.R., O’Neil, E.J.Jr., Lynds, C.R., Faber, S.M., Grillmair, C.J., Holtzman, J.A., & Light, R.M. 1995, *AJ*, 110, 2537
 Barmby, P., Huchra, J.P., Brodie, J.P., Forbes, D.A., Schroder, L.L., & Grillmair, C.J. 2000, *AJ*, 119, 727
 Bertin, E., & Arnouts, S. 1996, *A&AS*, 117, 393
 Brodie, J.P., Larsen, S.S., & Kissler-Patig, M. 2000, *ApJ*, 543, L19
 Dirsch, B., Richtler, R., Geisler, D., Forte, J.C., Bassino, L.P., & Gieren, W.P. 2003, *AJ*, 125, 1908
 Disney, M.J., & Wall, J.V. 1977, *MNRAS*, 179, 235
 Ferrarese, L., Côté, P., Jordán, A., Peng, E.W., Blakeslee, J.P., Piatek, S., Mei, S., Merritt, D., Milosavljevic, M., Tonry, J.L., & West, M.J. 2006, *ApJS*, 164, 334
 Fleming, D.E.B., Harris, W.E., Pritchett, C.J., & Hanes, D.A. 1995, *AJ*, 109, 1044
 Forbes, D.A., Faifer, F.R., Forte, J.C., Bridges, T., Beasley, M.A., Gebhardt, K., Hanes, D.A., Sharples, R., & Zepf, S.E. 2004, *MNRAS*, 355, 608
 Fukugita, M., Ichikawa, T., Gunn, J.E., Doi, M., Shimasaku, K., & Schneider, D.P. 1996, *AJ*, 111, 1748
 Geisler, D., Lee, M.G., & Kim, E. 1996, *AJ*, 111, 1529
 Girardi, L., Grebel, E.K., Odenkirchen, M., & Chiosi, C. 2004, *A&A*, 422, 205
 Harris, W.E. 2001, in *Star Clusters*, Saas-Fee Advanced Course 28, edited by L.Labhardt & B.Binggeli (Berlin: Springer-Verlag)
 Harris, W.E., Harris, G.L.H., Layden, A.C., & Stetson, P.B. 2007, *AJ*, 134, 43
 Harris, W.E., Kavelaars, J.J., Hanes, D.A., Hesser, J. E., & Pritchett, C.J. 2000, *ApJ*, 533, 137
 Harris, W.E., & Pudritz, R.E. 1994, *ApJ*, 429, 177
 Harris, W.E., Smith, M.G., & Myra, E.S. 1983, *ApJ*, 272, 456
 Harris, W.E., Whitmore, B.C., Karakla, D., Okon, W., Baum, W.A., Hanes, D.A., & Kavelaars, J.J. 2006, *ApJ*, 636, 90
 Hempel, M., Geisler, D., Hoard, D.W., & Harris, W.E. 2005, *A&A*, 439, 59
 Holtzman, J.A., Burrows, C.J., Casertano, S., Hester, J., Trauger, J.T., Watson, A.M., & Worthey, G. 1995, *PASP*, 107, 1065
 Jordán, A., McLaughlin, D.E., Côté, P., Ferrarese, L., Peng, E.W., Mei, S., Villegas, D., Merritt, D., Tonry, J.L., & West, M.J. 2007, *ApJS*, 171, 101
 Kundu, A., & Whitmore, B.C. 2001a, *AJ*, 121, 2950
 Kundu, A., & Whitmore, B.C. 2001a, *AJ*, 122, 1251
 Landolt, A.U. 1992, *AJ*, 104, 340
 Larsen, S.S., Brodie, J.P., Huchra, J.P., Forbes, D.A., & Grillmair, C.J. 2001, *AJ*, 121, 2974
 Lee, M. G., Kim, E. & Geisler, D. 1998, *AJ*, 115, 947
 MacDonald, P.D.M. 2007, documentation and code at <http://www.math.mcmaster.ca/peter/mix/mix.html>, Department of Mathematics and Statistics, McMaster University
 Maraston, C. 2005, *MNRAS*, 362, 799
 McLachlan, G.J., & Basford, K.E. 1987, *Mixture Models: Inference and Applications to Clustering*. Marcel Dekker, New York
 McLaughlin, D.E. 1999, *AJ*, 117, 2398
 McLaughlin, D.E., Harris, W.E., & Hanes, D.A. 1994, *ApJ*, 422, 486
 McLaughlin, D.E., Secker, J., Harris, W.E., & Geisler, D. 1995, *AJ*, 109, 1033
 Mieske, S., Jordán, A., Côté, P., Kissler-Patig, M., Peng, E.W., Ferrarese, L., Blakeslee, J.P., Mei, S., Merritt, D., Tonry, J.L., & West, M.J. 2006, *ApJ*, 653, 193
 Ostrov, P.G., Forte, J.C., & Geisler, D. 1998, *AJ*, 116, 2854
 Puzia, T. H., Kissler-Patig, M., Brodie, J. P., & Huchra, J. P. 1999, *AJ*, 118, 2734
 Rhode, K.L., & Zepf, S.E. 2001, *AJ*, 121, 210
 Richter, O.-G., Materne, J., & Huchtmeier, W.K. 1982, *A&A*, 111, 193
 Robin, A. C., Reylé, C., Derrière, S., & Picaud, S. 2003, *ã*, 409, 523
 Rothberg, B., Harris, W.E., Whitmore, B.C., Somerville, R., & Cockcroft, R. 2007, *ApJ*, submitted
 Secker, J., Geisler, D., McLaughlin, D.E., & Harris, W.E. 1995, *AJ*, 109, 1019
 Spitler, L.R., Larsen, S.S., Strader, J., Brodie, J.P., Forbes, D.A., & Beasley, M.A. 2006, *AJ*, 132, 1593
 Strader, J., Brodie, J.P., & Forbes, D.A. 2004, *AJ*, 127, 3431
 Strader, J., Brodie, J.P., Spitler, L., & Beasley, M.A. 2006, *AJ*, 132, 2333
 Tamura, N., Sharples, R.M., Arimoto, N., Onodera, M., Ohta, K., & Yamada, Y. 2006, *MNRAS*, 373, 588
 Vasterberg, A.R., Jorsater, S., & Lindblad, P.O. 1991, *A&A*, 247, 335
 Wehner, E.H.M., & Harris, W.E. 2007, *ApJ*, in press (astro-ph/0708:1514)
 Zepf, S.E., & Ashman, K.M. 1993, *MNRAS*, 264, 611
 Zinn, R. 1985, *ApJ*, 293, 424